metals

MDPI

*Article*

# Proposal and Assessment of a Multiple Cycle-Continuous Cooling Transformation (MC-CCT) Diagram for Wire Arc Additive Manufacturing of Thin Walls

**Mats Högström, Amirhosein Fadaei, Amin Rahimi, Peigang Li, Mattias Igestrand, Joel Andersson and Americo Scotti ***

Department of Engineering Science, University West, SE-461 86 Trollhättan, Sweden;
mats.hoegstroem.ext@siemens-energy.com (M.H.); amir.fad1990@gmail.com (A.F.);
amin.rahimi64@gmail.com (A.R.); mattias.igestrand@hv.se (M.I.); joel.andersson@hv.se (J.A.)
* Correspondence: americo.scotti@hv.se

**Abstract:** Continuous cooling transformation (CCT) diagrams of base metals are common in welding. They can be built using physical or numerical simulations, each with advantages and limitations. However, those are not usual for weld metal, considering its variable composition due to the dilution of the weld into the base metal. Wire Arc Additive Manufacturing (WAAM) is a distinctive case in which the interest in materials comparable with weld composition raises attention to estimating their mechanical properties. Notwithstanding, this concept is still not used in WAAM. Therefore, the aim of this work was to address a methodology to raise MC-CCT (Multiple Cycle Continuous Cooling Transformation) diagrams for WAAM by combining physical and numerical simulations. A high-strength low-alloy steel (HSLA) feedstock (a combination of a wire and a shielding gas) was used as a case study. To keep CCT as representative as possible, the typical multiple thermal cycles for additive manufacturing thin walls were determined and replicated in physical simulations (Gleeble dilatometry). The start and end transformations were determined by the differential linear variation approach for each thermal cycle. Microstructure analyses and hardness were used to characterise the product after the multiple cycles. The same CCT diagram was raised by a commercial numerical simulation package to determine the shape of the transformation curves. A range of austenitic grain sizes was scanned for the curve position matching the experimental results. Combining the experimental data and numerically simulated curves made estimating the final CCT diagram possible.

**Keywords:** CCT diagram; WAAM; physical simulation; numerical simulation

check for updates

**Citation:** Högström, M.; Fadaei, A.; Rahimi, A.; Li, P.; Igestrand, M.; Andersson, J.; Scotti, A. Proposal and Assessment of a Multiple Cycle-Continuous Cooling Transformation (MC-CCT) Diagram for Wire Arc Additive Manufacturing of Thin Walls. *Metals* **2023**, *13*, 1533. https://doi.org/10.3390/met13091533

Academic Editor: Antonello Astarita

Received: 24 July 2023
Revised: 19 August 2023
Accepted: 27 August 2023
Published: 29 August 2023

## 1. Introduction

Continuous Cooling Transformation (CCT) diagrams of base metals are fundamental in arc welding to predict the metallurgical behaviour of the plates under different heat inputs (thermal cycles). A CCT diagram was defined in the introduction of Trzaska et al. [1] as a quantitative microstructure and hardness dependence on the temperature and time of the supercooled austenite transformations. Locations and shapes of the supercooled austenite transformation curves, plotted on the CCT diagrams, depend mostly on the chemical composition of the steel, extent of austenite homogenising, austenite grain size, as well as austenitizing temperature and time. According to Alexandrov and Lippold [2], the ranges of welding conditions that provide an optimal combination of microstructural constituents concerning weldability and mechanical properties are determined by CCT diagrams. The current literature is rich in papers dealing with CCT diagrams for welding, mainly for steel, where an atlas presented by Atkins [3] belongs to the most traditional work. Regardless of their usability value, CCT diagrams are not very popular outside of the academic environment since the construction of charts is time- and resource-consuming (usually critical applications, like nuclear plants, use these diagrams). But interest in this experimental approach tends to increase with novel manufacturing technologies.

It is a fact that CCT diagrams for weld metals are scarcely known, even in academic work, because the consumables mix up with the base metal in variable degrees depending on the weld process parameters—the final weld metal takes different compositions, and a diagram for each unlimited composition would be needed. However, wire arc additive manufacturing (WAAM) and other additive manufacturing technologies differ from welding. The feedstock composition (mainly due to the wire and powder but also to the shielding gas) is the build composition, regardless of the arc energy and parameters, keeping it practically constant (neglecting variation of segregation across the build). And, in the same way as base metals, the mechanical properties are related to the microstructures. Therefore, knowing the cooling rate (which is possible to estimate by numerical simulation or dedicated measurement techniques), a CCT diagram of the WAAM deposit composition would help the end-user predict the final microstructure of the build (it would be useful to receive CCT diagrams from the suppliers).

Kellog et al. [4] cite that the microstructure of parts fabricated via additive manufacturing (AM) is usually not the same as that of their conventionally manufactured counterparts. To study such differences, the authors (joining the interests of academia, a research center, and companies) recently (2022) compared the weldability characteristics of powder bed fusion AM and wrought materials. Despite the fact that they found interesting results, they physically simulated HAZ (heat-affected zone), but they have not built a CCT diagram for the deposited material.

As far as the knowledge of the present paper's authors is concerned, only in 2023 (in a concurrent period to the research from which this current paper was generated) did researchers publish about the CCT diagram's usage in AM. These studies still have drawbacks if WAAM of thin wall phase evolution assessment is the target. Halmešová et al. [5], for instance, determined a CCT diagram (using dilatometry) with extended information about strength, ductility, and the estimated value of the work-hardening coefficient. Laser-directed energy deposition (L-DED) and selective laser melting (SLM) processes were used, but not WAAM. In addition, although multiple layers were used to build the parts for taking dilatometer test samples, the authors used only a single austenitising temperature in the physical simulation at different cooling rates. It means that the potential multiple-cycle effect on the microstructure's evolution was not taken into account. Mishra et al. [6] also raised and used a CCT diagram to discuss their study on a model to predict the relation between the thermal history from WAAM and solid-state phase transformations in a high-strength low-alloy steel (HSLA) deposition material. Although they have used a very consistent experimental approach and reached important conclusions, the raised CCT diagram also presented deviations from actual layer depositions. They were able to measure the multiple thermal cycles. However, instead of imposing similar thermal cycles in the dilatometer, the samples to build the CCT diagram were, justifiably, heated to 900 °C at 20 °C/s and held at 900 °C for 120 s for full austenitisation. Similarly to Halmešová et al.'s work, the effects of heating time and multiple transformations to austenite and back to typical HSLA steel microstructures on the final microstructure were neglected.

It is important to state that WAAM has other intrinsic characteristics that distance it from welding and from the abovementioned publications [5,6], which are more pronounced when building thin walls, where the microstructure architecture is unique (due to a heat flux that is almost unidirectional from top to bottom). This characteristic is the result of multiple cycles imposed by subsequently deposited layers. It means that each subsequent layer will be, totally or partially, thermally heat treated several times at different peak temperatures (the last heat treatment likely represents normalising or intercritical Heat Affected Zone (HAZ) regions, not disregarding the sub-critical region and the consequent tempering effect). This reheat treatment will also affect the microstructural evolution in a CCT diagram, since any CCT diagram depends on the austenitising temperature (peak temperatures of the WAAM thermal cycles) and the prior-to-cooling austenitic grain sizes. Gutiérrez Castañeda et al. [7] emphasise that most CCT diagrams in steels are from temperatures where austenite is the stable phase (full austenitisation), which does not allow a precise estimation of the microstructures resulting from some processing routes. This statement applies to the last reheat treatment during WAAM for thin walls and their multiple cycles. Hence, a CCT diagram for WAAM applications is hereafter named "multiple cycle continuous cooling diagrams," referred to by the acronym "MC-CCT."

In time, it is worth remembering that bulky wire arc additively manufactured builds allow more 3D heat flux, and the effect of one layer over the previous one differs from that of thin wall builds. Bulky builds resemble, to some extent, the "tempering pass" technique, whose outcome was reported, among others, by Cruz-Crespo et al. [8]. The tempering pass, in turn, resembles the effect of one layer over the other in WAAM, but it is not precisely a multiple-cycle effect.

As remarked above, constructing a CCT diagram is not a simple task. The most popular approach is through experimentation (physical simulation), based either on dilatometry (see, for instance, Zong and Liu [9]) or differential analyses of the cooling temperature (as described by Zachrisson [10] and Cruz-Crespo et al. [8]), followed by metallographic examinations and hardness testing. Dilation methods can use Joule heating and a diametral sensor, as employed in Gleeble®, or inductive coil furnace heating and mechanical contact or non-contact optical charge-coupled device (CCD sensors), as in fast (quenching) dilatometers (such as those used in Moravec et al. [11]). The method used in dilatometry, regardless of the heating method, is based on plotting the differential linear variation (dL/L) of the sample under heating and cooling as a function of time.

A second means of creating CCT diagrams is through numerical simulations. Thermophysical and physical properties are complexly modelled in such a way as to predict, among other properties, the transformation temperatures of an austenitising material at different cooling rates. Calculation methods offer an alternative to experimental measurement. Guo et al.'s [12] paper describes the models incorporated in a commercial package, JMatPro®, for calculating phase transformations. According to these authors, the success of the model is based on an accurate description of all the major phase transformations taking place as well as an accurate calculation of the properties of different phases formed during the heat treatment process. Trzaska et al. [1] presented numerical methods for calculating anisothermal diagrams of supercooled austenite based on physical, statistical, or artificial intelligence methods. The results of the calculations consisted of the temperatures at the beginning and end of a particular transformation, the volume fraction of structural components, and the hardness of steel after heat treatment. Recently, Collins et al. [13] proposed a model for predicting the CCT behaviour of low-alloy steels using semi-empirical expressions for isothermal transformation. Collins et al. still cite that some of the more popular software packages include JMatPro, Thermo-Calc, and MAP_STEEL_MUCG83. From all the above citations, there is an agreement that all methods are prone to inaccuracies due to different reasons. For the specific case of the multiple cycle WAAM, estimating the austenitizing grain size as a function of the peak temperature, an input to the models, is challenging.

Even though it is a simulation, physical simulation (as used with Geeble or fast dilatometers) is a financially resource-consuming technology. To physically simulate WAAM-related material by this means, there are costs associated with specimen fabrication (wall building, specimen withdrawing, and machining) and operation costs (equipment, personnel, etc.). These costs increase with the required number of samples; a comprehensive CCT diagram requires a great quantity of specimens to scan all microstructural fields. The numerical simulation would be a solution to reduce costs concerning the microstructure's representability for a CCT diagram. However, numerical simulations have intrinsic uncertainties. A balance between costs and uncertainties could be reached by joining physical and numerical simulations. Therefore, this work aimed to propose and assess a methodology to raise MC-CCT diagrams for WAAM by combining physical and numerical simulations.

## 2. Methodology

The procedures for elaborating conventional CCT diagrams (Adonyi & Blodgett [14] and Roshan et al. [15], amongst several others) were used as the basis of this work. Thus, the principles of dilatometry and physical simulation (Gleebe®, Dynamic Systems Inc., Poestenkill, NY, USA) were used to detect phase transformations during cooling under typical WAAM multiple thermal cycles. However, in such a study, several other boundary conditions were observed. Material samples were taken from additively manufactured walls rather than from same-class wrought material to preserve the chemical composition after welding arc processing and the solidification history of the target steel as much as possible. It has been observed that the dilution between each couple of layers is usually high (40% to 60%) in the thin wall approach of WAA-manufactured HSLA walls (one track per layer). Therefore, along a large extent of the wall height from which the samples were taken, a given portion of the material was already metallurgically influenced by multiple thermal cycles imposed during the wall's construction.

Observing Figure 1, one can expect all layers underneath the 3rd or 4th layer from the top layer to undergo several thermal cycles. It means that the metallurgical changes realised by the first thermal cycle over the previous layer are modified by subsequent thermal cycles with progressively lower peak temperatures. By the end, a way-down layer (distance depending on the energy and layer volume) in the wall-building direction will have transformed at a peak temperature just above the transformation temperature for the given steel (usually referred to as the normalising temperature) or within its inter-critical temperature range. And the layers below that position (sub-critical temperature range) will have the transformed material heated again a couple of times, yet below the transformation temperature. Some stress relief, hard-phase tempering, and delayed transformations (retained austenite, for instance) might occur, depending on the time span the material portion is maintained at the normalising and subcritical region temperatures for the given steel.

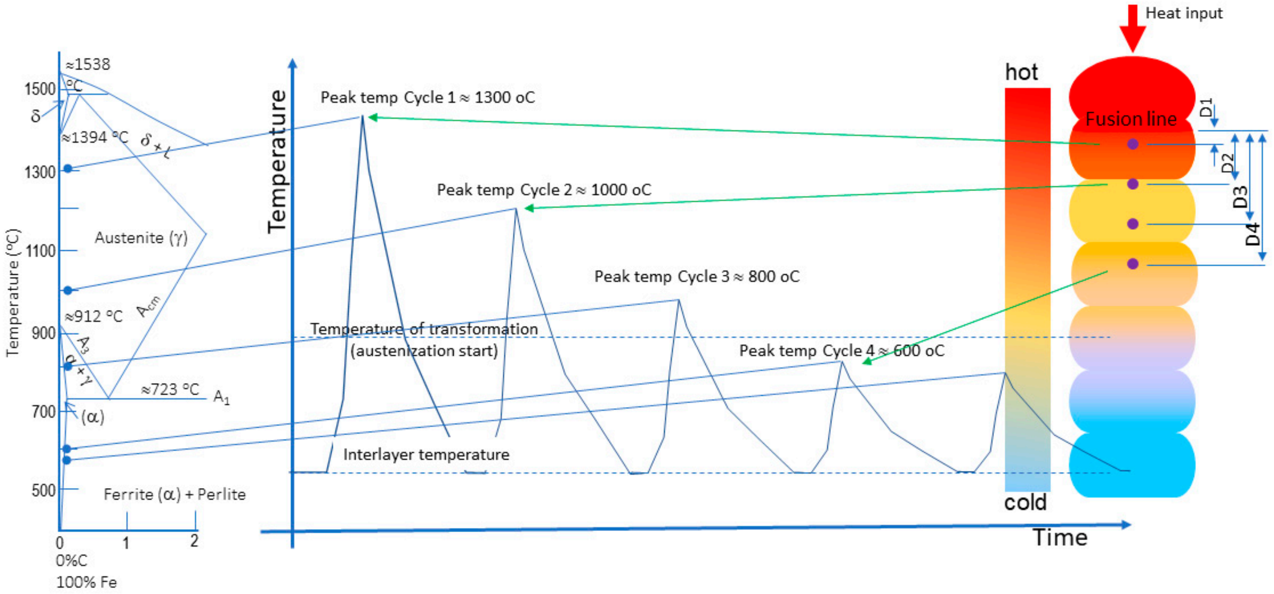

**Figure 1.** Schematic to represent the effect of multiple thermal cycles over the peak temperature and corresponding phase transformations during heating at different positions along the wall-building direction (the phase diagram, temperature distances for the thermal cycle measurements, and thermocycle shapes are hypothetical and used only for illustration).

It is important to state that in physical simulation, it is very difficult to reproduce liquid-to-solid transformations. Therefore, the planned thermal cycles for the physical simulation in this work were designed to mimic the behaviour illustrated in Figure 1. It means that, after the multiple thermal cycles enforced in the samples, the material is, in practice, thermally retreated again (the original metallurgical history of the material is lost, but chemical composition variation by the arc and the solidification-induced microsegregation that may further complicate the phase transformations on cooling are roughly maintained).

However, metallurgical transformations in WAAM do not depend only on the peak temperature, composition, and thermal history of the material (homogenisation and microsegregation), but also on the whole thermal cycle. As schematised in Figure 2, the cooling rates of each thermal cycle, conventionally from 800–500 °C for HSLA steels, govern the microcomponent at room temperature (the object of a CCT diagram). The heating rates determine the time during heating that the temperature is above the transformation temperature, causing grain coarsening and influencing the material quenchability process. Lan et al. [16] studied and demonstrated the effect of austenite grain size on the Bainite transformation. Actual welding thermal cycles do not contain a holding (soaking) time at the peak temperatures (Scotti et al. [17]), which, when imposed in thermal simulation, also represents grain coarsening before cooling. The heating and cooling rates (not only the latter) depend on the actual heat input; higher heat input results in longer cooling and heating times, and vice versa.

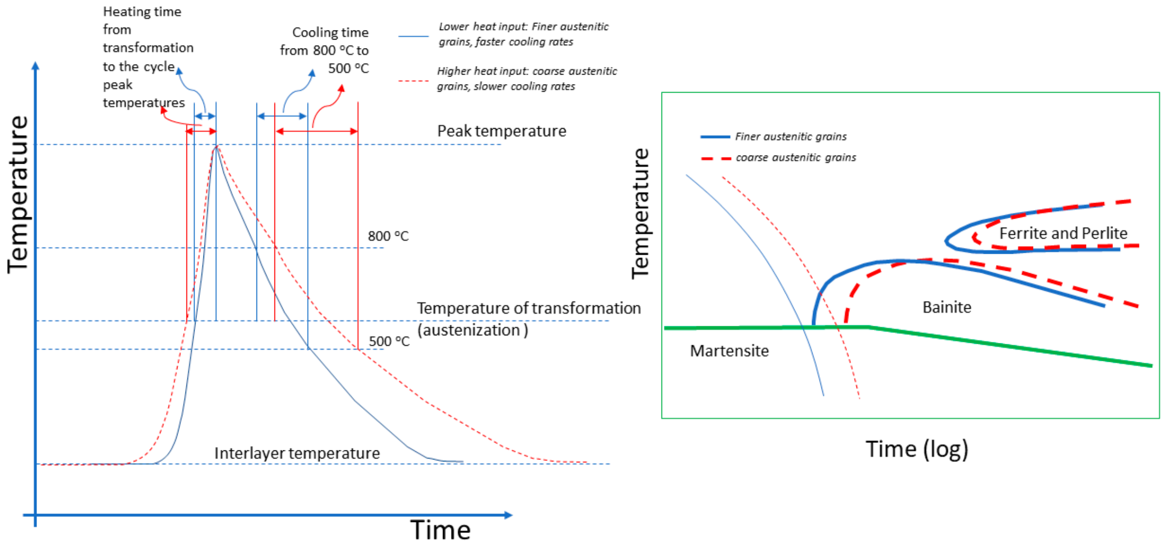

**Figure 2.** Scheme to show the influence of heating and cooling rate on grain coarsening and quenchability of HSLA steels (on the right, 100% Martensite may exist even with a slower cooling rate, due to the austenitic grain coarsening and consequence delay of phase transformations).

To address the above mentioned in the working plan, the experiments for determining MC-CCT diagrams were settled considering the cited boundary conditions. For physical simulations and dilatometry, a Gleeble 3800 was employed. The cross-section dilations and contractions were measured at the centre of the sample, where the thermal cycles were imposed, by clipping on a 39018 C-Gauge (LVDT type gauge) with ±0.4 µm of resolution. The temperature at the central Gleeble specimens was measured (and controlled to follow the desirable thermal cycle) with a K-type 0.25-mm-wire diameter (30 AWG) commercial thermocouple (nominal accuracy of 3%) on their cylindrical surface. To achieve a fast dynamic response of the temperature measurements, besides the small diameter of each thermocouple wire, a minimal-sized connection between the thermocouples and the wall surface was forced by welding each leg separately. Details of the dilatometry sample acquisition and dimensioning are given ahead. Several thermal cycles typical of WAAM for thin walls of carbon steel were applied to cover an extensive range of cooling rates (always keeping the proportionality between the cooling and heating curves).

The decision to keep this cooling/heating intercorrelation in the experimental thermal cycles is supported by Barrick et al. [18], who mentioned that the heating rate changes the $A_3$ temperature of steels, and Moravec et al. [11], who also observed higher $A_1$ and $A_3$

transformation temperatures with increasing heating rates. The determination procedure of the transformation start and end temperatures was the standard (such as used in Zong & Liu [9] and Krbat'a et al. [19]), i.e., the linear part of the cooling curve is identified, and a tangent parallel to it is drawn beyond the point where the curves start to bow, below and above the start and finish of the transformation regime, respectively. The transformation start and finish temperatures are determined where the curves begin to deviate from linearity, i.e., when the slope of the dilation/contraction traces (over time) diverges from a linear curve, and the transformation ends when the slope returns to linearity. Figure 3 illustrates the dilatometric curves of a sample at each of the four multiple cycles. Note that under the 3rd cycle, the transformation during heating was not complete (intercritical region, as suggested in Figure 1), and that there is no transformation under the 4th cycle (subcritical region, as also indicated in Figure 1).

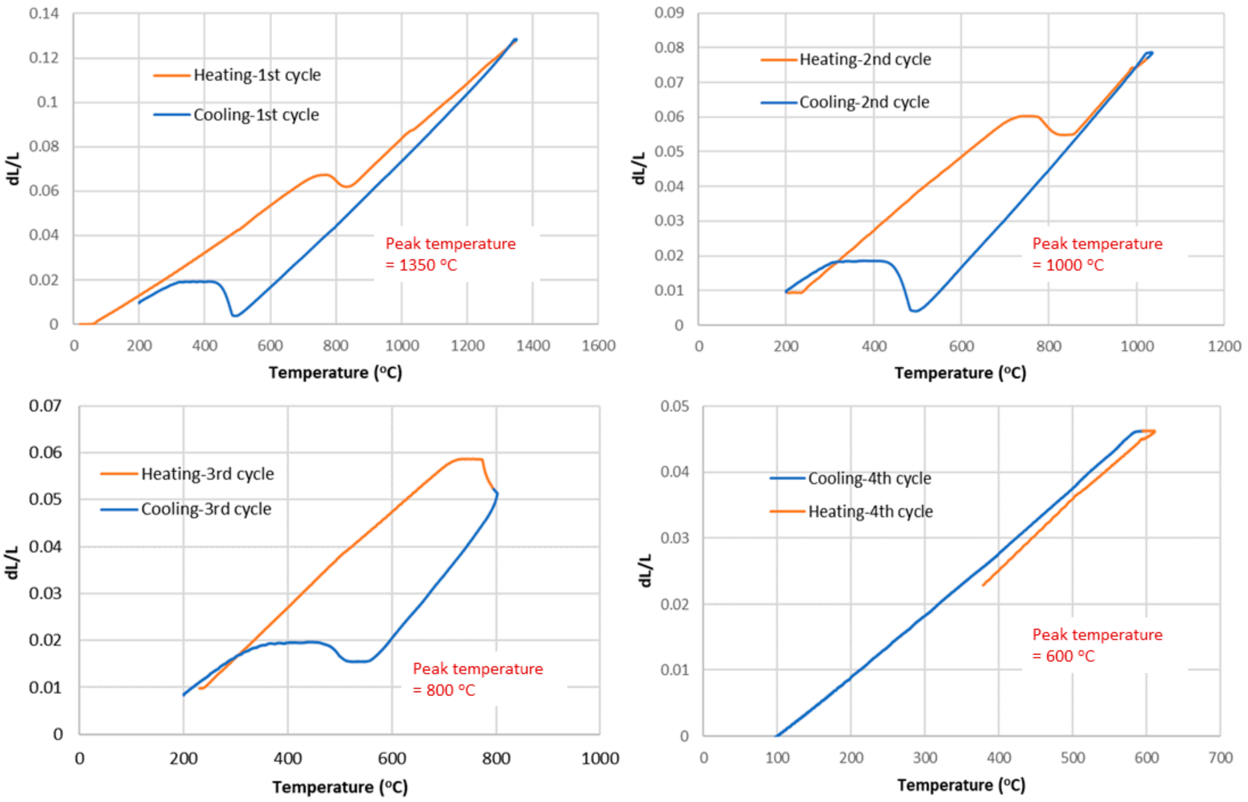

**Figure 3.** Typical dilatometric curve during heating and cooling, used for the determination of start and end transformation temperatures, where dL/L is the differential linear variation (dl/L) of the sample diameter as a function of cooling time given in seconds.

Each central point specimen cross-section was metallographically prepared and analysed using optical microscopy (OM) and a microhardness tester. The sample metallurgical characterisations and the cooling curves were superimposed on CCT diagrams numerically simulated to support the construction of the MC-CCT of this material with fewer experiments. The numerical simulation was done using a commercial package (JMatPro, JMatPro® software, ver. 13.0, Sente Software Ltd, Guildford, UK which provides technical information at https://www.sentesoftware.co.uk/site-media/jmp-flyer-150409, accessed on 5 July 2023). The numerically simulated CCT diagrams considered different peak temperatures to mimic the microstructures at different positions along the wall-building direction. Several CCT diagrams were numerically simulated at the same peak temperature, but different initial grain sizes were used to make up for the unknown initial grain size at each peak temperature. Then, an adaptative process was devised to point out the likely grain size.

## 3. Experimental Development

### *3.1. Material, Processing and Sampling*

The MC-CCT diagram was developed for an HSLA steel resulting from WAA-manufactured deposits carried out with 1.2-mm-diameter metal-cored wire (OK Tubrod 14.03 from ESAB), shielded by a blend of Ar + 5%$CO_2$. The manufacturer recommends this wire for high-strength applications (>690 MPa), classification SFA/AWS A5.28 E110C-G, and EN ISO 18276-A T 69 4 Mn2NiMo M M 2 H10. Table 1 presents the representative chemical composition of the layers after deposition. The reasonably low $CO_2$ content in the shielding gas was purposely chosen to balance penetration and an oversized pool. A CMT (cold metal transfer) version of GMAW (gas metal arc welding) was used to build the wall, assisted by an ABB IRB2600 robot, whose settings and resultant parameters are shown in Table 2.

**Table 1.** Average chemical composition (in wt%) from 3 walls built with the wire OK Tubrod 14.03 (steel under study) shielded by Ar + 5%$CO_2$.

| C | Mn | Si | Cr | Ni | Mo | P | S | W | Co | V |
|---|---|---|---|---|---|---|---|---|---|---|
| 0.122 | 1.803 | 0.547 | 0.017 | 2.317 | 0.550 | 0.008 | 0.008 | 0.006 | 0.007 | 0.010 |
| Nb | Ti | Cu | Al | B | N | O | Residual (Sn, Pb, As, Sb, Zr, Zn) | | | |
| 0.006 | 0.006 | 0.012 | 0.015 | 0.001 | 0.003 | 0.054 | <0.017 | | | |

**Table 2.** Welding conditions used to manufacture the wall for dilatometry specimen sampling.

| **Power Source** | **Fronius TPS 500i CMT** |
|---|---|
| Synergic line | 3861 |
| Torch | MTB 500i |
| Torch angle | 90° (perpendicular to the wall top surface) |
| CTWD (mm) | 16–17 |
| Set WFS (m/min) | 4.6 |
| Set Travel speed (mm/s) | 5 |
| Average current (A) | 156.6 |
| Average voltage (V) | 15.2 |

For sampling specimens for the physical simulation using Glebble, a 10-mm-wide wall was built (110 mm high and 250 mm long) over a plain carbon steel substrate positioned in the upright position (the substrate was 10-mm thick to serve as a pre-wall and maintain approximately the same heat flux as the first layers). See view (a) in Figure 4 for the fixture and pre-wall schematic and (b) for the walls. After discarding 20 mm from each wall end, its usable length was sliced into pieces (Figure 4c) for subsequent machining (turning) into cylindrical specimens ($\Phi$ 6 mm × 110 mm long). This diameter was chosen to keep a balance between dilatometry sensitivity (the larger the diameter, the more sensitive the measurement with the C-gauge would be) and heating time (the larger the diameter, the longer it takes to heat the centre of the specimen).

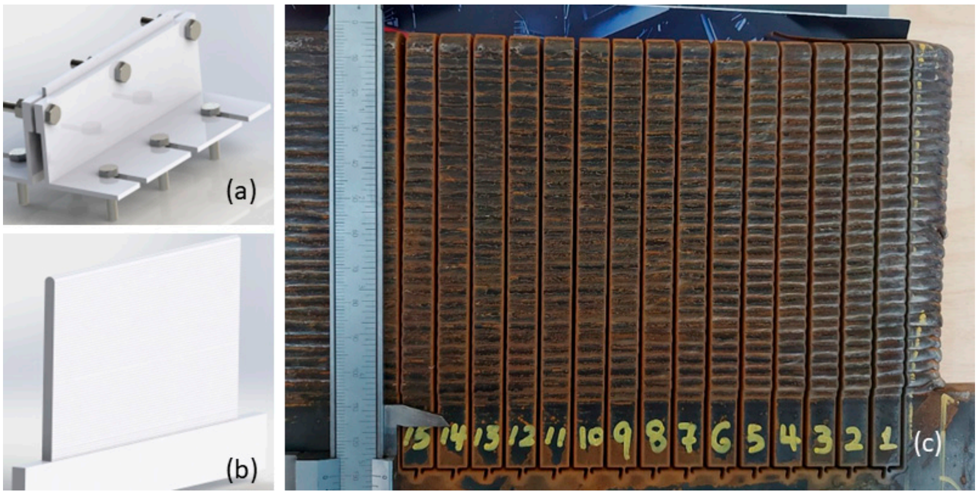

**Figure 4.** Schematics of the fixture and pre-wall (**a**) and the building wall (**b**), and the wall sliced (**c**) for machining the Gleeble specimens.

### 3.2. *Designing of the Thermal Cycles*

Gleeble requires the thermal cycles planned to be imposed on the specimens to be written as a script. Initially, K-type 0.25-mm-wire-diameter commercial thermocouples were inserted (with a nominal accuracy of 3%) on the top of one of the wall layers WAA. manufactured with different arc energies while keeping the same wall width. Besides the small diameter of each thermocouple wire, a voluminous junction between the thermocouples and the wall surface was again avoided (each leg was separately welded) to achieve a fast dynamic response to the temperature measurements. three thermocouples per wall, to ascertain by interpolation the proper distance of them concerning the layer under depositions and obtain the temperature × time curves as real as possible. These thermocouples acquired the actual multiple thermal cycles that the subsequent layers imposed on the position of the thermocouples from the three walls. The multiple thermal cycles were recorded, and their metrics were used as a reference to elaborate the first three Gleeble scripts. Then, multiple thermal cycles composed of four peak temperatures were arbitrarily defined to represent the thermal history of a material portion at the middle wall height under the subsequent peak temperatures, namely 1300 °C, 1000 °C, 800 °C, and 600 °C (with no soaking time at the peaks), the latter below the transformation temperature (see in Figure 1 that these temperatures represent critical fields in the hypothetical phase diagram of the material).

It is important to mention that numerical simulation of the phase diagram using the average chemical composition of the 3 walls (Table 1) predicted $A_1$ and $A_3$ temperatures below those suggested in Figure 1 (which are not actual for the steel under study in this work). Based on this phase diagram, some austenisation is expected (some transformation would occur) at a peak temperature of 600 °C. At the peak temperature of 800 °C, the material would already be fully austenitic and not within the intercritical region. However, as heating in WAAM is much faster than in phase diagrams, one can expect higher temperatures for both $A_1$ and $A_3$ [14,18]. Figure 3 also supports that there is no complete transformation when the peak temperature is 800 °C, and no transformation, or a minimal amount, when the peak temperature is 600 °C.

Each thermal cycle within each chain was designed to cool up to 200 °C (instead of room temperature) to make the total simulation faster, considering that no metallurgical transformation could occur below this temperature for the given steel. However, the thermal cycles had to cover a range of cooling rates as wide as possible to build the MC-CCT diagram, keeping the same multiple peak temperatures. To overcome this challenge, dummy specimens were used to find the appropriate Gleeble set parameters. The jaw span and knob power position were systematically varied. The higher the power, the faster the heating. A long jaw span would also make the heating time faster but the cooling slower (this concurrent behaviour does not favour experimental planning since, as seen in Figure 2, a shorter heating time should be followed by a shorter cooling time). As a result, the best compromise to fit typical thermal cycles from WAAM of HSLA steel when using this material and specimen dimension was with a jaw span of 30 mm and the power knob at position 3. These settings provided a minimum Δt 500-peak °C (heating) = 0.98 s and a minimal cooling time from 800 to 500 °C of 14.6 s (no forced cooling was employed to avoid a significant thermal gradient across the specimen cross-section, observed by Kardoulaki et al. [20], which would affect the dilatometric measurement).

Using these Gleeble settings and the three experimentally raised thermal cycle curves, extrapolations were employed to draw more curves (faster and slower), assisted by FEM simulation. In the extrapolations, there was a proportional variation in the curve slopes. However, there was demand for even faster cooling rates so that Martensite could be reached. To accomplish this latter demand, 2 specimens were re-machined to reduce their cross-section area at their centres (to a Φ of 4 mm × 15 mm long). In addition, the cooling was forced to the maximum by programming a script with faster cooling than possible. The scripts generated for 12 specimens are illustrated in Figure 5.

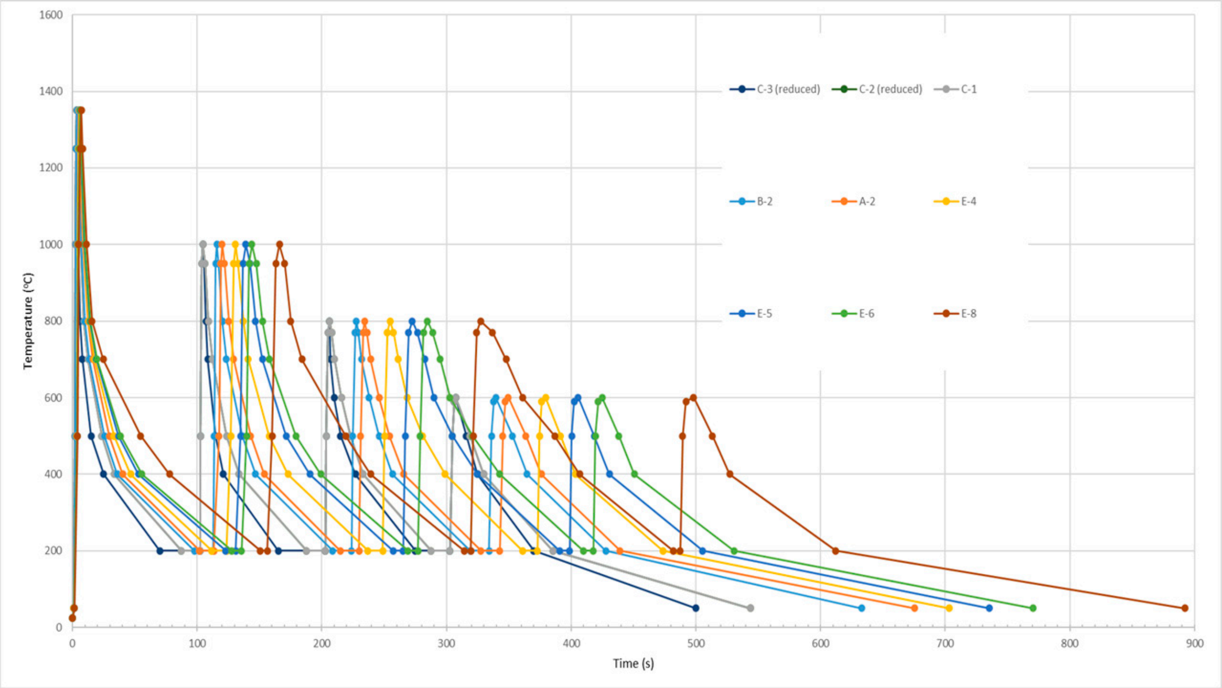

**Figure 5.** The programmed curves according to the scripts used in the Gleeble simulation of multiple cycles in 9 specimens.

Table 3 presents the metrics of the programmed thermal cycles. As seen in this table, progressively decreasing heating and cooling rates were programmed for the specimens from C-3 (reduced) to E-8. It is also seen that the faster thermal cycle from the C-3 (reduced), which corresponds to a simulated low heat input, reached a cooling rate from 800–500 °C of 33.71 °C/s at the 3rd cycle (whose peak temperature was still above the austenitising temperature), while the slowest thermal cycle (E-8), mimicking a high heat input, reached a cooling rate from 800–500 °C of only 5.04 °C/s at the 3rd cycle. These quantities show that an extended range of cooling rates was covered.

**Table 3.** The metrics (heating and cooling times and rates) from the programmed thermal cycles of Figure 5.

| | | | Heating | | Cooling | | | |
|---|---|---|---|---|---|---|---|---|
| **Reference Number** | **Cycle** | **Peak Temp (°C)** | **Δt 500-Peak (s)** | **Rate from 500-Peak (°C/s)** | **Δt Peak-800 (s)** | **Rate from Peak-800 (°C/s)** | **Δt8-5 (s)** | **Rate from 800–500 (°C/s)** |
| C-3 (reduced) | 1st | 1350 | 1.28 | 664.06 | 2.83 | 194.48 | 9.00 | 33.33 |
| | 2nd | 1000 | 1.93 | 259.61 | 2.32 | 86.24 | 8.00 | 37.50 |
| | 3rd | 800 | 2.65 | 113.21 | | | 8.85 | 33.91 |
| | 4th | 600 | 2.70 | 37.04 | | | | |
| C-2 (reduced) | 1st | 1350 | 1.28 | 664.06 | 5.98 | 92.02 | 14.45 | 20.77 |
| | 2nd | 1000 | 1.93 | 259.61 | 4.37 | 45.76 | 14.69 | 20.42 |
| | 3rd | 800 | 2.65 | 113.21 | | | 16.79 | 17.87 |
| | 4th | 600 | 2.70 | 37.04 | | | | |
| C-1 | 1st | 1350 | 1.28 | 664.06 | 5.98 | 92.02 | 14.45 | 20.77 |
| | 2nd | 1000 | 1.93 | 259.61 | 4.37 | 45.76 | 14.69 | 20.42 |
| | 3rd | 800 | 2.65 | 113.21 | | | 16.79 | 17.87 |
| | 4th | 600 | 2.70 | 37.04 | | | | |
| B-2 | 1st | 1350 | 1.44 | 590.28 | 6.19 | 88.85 | 15.86 | 18.92 |
| | 2nd | 1000 | 1.93 | 259.61 | 4.48 | 44.68 | 16.18 | 18.54 |
| | 3rd | 800 | 3.00 | 100.00 | | | 18.24 | 16.45 |
| | 4th | 600 | 3.48 | 28.74 | | | | |
| A-2 | 1st | 1350 | 1.67 | 508.98 | 7.33 | 75.04 | 17.06 | 17.58 |
| | 2nd | 1000 | 1.93 | 259.61 | 5.49 | 36.43 | 17.48 | 17.16 |
| | 3rd | 800 | 3.18 | 94.34 | | | 20.12 | 14.91 |
| | 4th | 600 | 4.39 | 22.78 | | | | |
| E-4 | 1st | 1350 | 2.05 | 414.63 | 7.55 | 72.85 | 20.00 | 15.00 |
| | 2nd | 1000 | 3.50 | 142.86 | 6.40 | 31.25 | 20.80 | 14.42 |
| | 3rd | 800 | 4.40 | 68.18 | | | 26.30 | 11.41 |
| | 4th | 600 | 4.90 | 20.41 | | | | |
| E-5 | 1st | 1350 | 2.30 | 369.57 | 8.00 | 68.75 | 23.00 | 13.04 |
| | 2nd | 1000 | 4.00 | 125.00 | 7.90 | 25.32 | 24.50 | 12.24 |
| | 3rd | 800 | 5.60 | 53.57 | | | 32.20 | 9.32 |
| | 4th | 600 | 5.10 | 19.61 | | | | |
| E-6 | 1st | 1350 | 2.39 | 355.65 | 8.25 | 66.67 | 24.30 | 12.35 |
| | 2nd | 1000 | 4.30 | 116.28 | 8.30 | 24.10 | 26.80 | 11.19 |
| | 3rd | 800 | 5.80 | 51.72 | | | 36.00 | 8.33 |
| | 4th | 600 | 5.30 | 18.87 | | | | |
| E-8 | 1st | 1350 | 3.30 | 257.58 | 8.60 | 63.95 | 39.00 | 7.69 |
| | 2nd | 1000 | 5.80 | 86.21 | 9.00 | 22.22 | 44.00 | 6.82 |
| | 3rd | 800 | 6.00 | 50.00 | | | 59.50 | 5.04 |
| | 4th | 600 | 8.90 | 11.24 | | | | |

### *3.3. Supplementing the Experimental Approach*

To start, numerical simulations using the commercial software package JMatPro® were employed to raise CCT diagrams utilising the steel chemical composition and varying the peak temperature as well as the initial austenitic grain sizes. The objective was to demonstrate the effect of these factors on the expected microstructure and to mimic the different regions of the material under multiple thermal cycles (Figures 1 and 2). In addition, some extra physical simulations were devised to support the reliability of the proposed methodology (Section 2) and experimental development (Sections 3.1 and 3.2). The first was to carry out the Gleeble simulation on three unused specimens to measure the progress of the multiple thermal cycles. For that, the same Gleeble set parameters used for specimen A-2 (see Table 3) were replicated, but only the 1st cycle was applied in the first extra specimen, the 1st and 2nd cycles in the second specimen, and the 1st, 2nd, and 3rd cycles in the third additional specimen. The expected outcome would be grain downsizing and respective microstructural changes.

Finally, reaching very fast cooling in Gleeble for the CCT diagram procedure is challenging. To force a cooling rate faster than those possible with the planned thermal cycles in Figure 5, the material samples (approximately 30-mm-long × 6-mm-diameter) were heated at a given peak temperature (1000 °C) in a furnace and quenched by different means (water at room temperature, air at room temperature, and air inside the furnace). The temperature of 1000 °C was chosen because it was the lowest one in the Gleeble simulation at which full austenitisation would occur. The objective was to demonstrate metallurgical variations in such extreme cooling rates (faster and slower than could possibly be achieved with the Gleeble) to be compared with the cooling imposed on the Gleeble specimens. The comparison of macrostructures and hardness between these samples and those from the fastest and slowest cooled specimens from Table 3 (C-3 (reduced) and E-8, respectively) could indicate whether the microstructures reached in the physical simulation were coherent.

## 4. Results and Discussions

### 4.1. The Effect of Cooling Rates on the Position of the Transformation Curves in the CCT Diagram

Figure 6 presents the optical microscope (OM) images of the specimen cross-sections (located at the middle of the specimen length, where the temperature was under control) and the respective Vickers averaged hardness (out of 20 indentations). As seen, there are no significant differences in the OM microstructures (predominately bainitic) and hardness for a range of cooling rates from ≈4.5 °C/s to 18 °C/s. Bainite transformation has been deeply studied by Prof. Bhadeshia, and the readers are suggested to consult his work [21]. Zong and Liu [9] also found that Bainite occurs in a similarly wide range of cooling rates (2–20 °C/s) when physically simulating a micro-alloyed and quenched E550-class steel. In this range, these authors showed that the microstructure consisted mainly of lath and granular Bainites. The proportion of lath Bainite increased and granular Bainite decreased as the cooling rate increased, similar to the results presented in Figure 6. However, the hardness in Figure 6 became slightly higher for the cooling rate from 800 to 500 °C (CR8–5) of 33.0 °C/s, suggesting the presence of Martensite at this fastest cooling.

Table 4, in turn, provides the start and end transformation temperatures during the 3rd thermal cycle in each specimen, measured from the dilatometric curves. According to Gutiérrez Castañeda et al. [7], two microstructural events occur during continuous heating, recrystallisation and ferrite-to-austenite phase transformation. As seen, there are no clear trends in the start austenitisation temperatures concerning the heating rate in the range of thermal cycles reached in this work. There are also no clear trends in the starting transformation temperatures concerning the cooling rate. This result contradicts Moravec et al. [11], for whom the austenite decomposition start temperatures have a decreasing trend with an increasing cooling rate (yet with a more quenchable material and in a wider range of cooling rates, from 0.03 to 100 °C/s). However, it was observed in Table 4 that the end transformation temperatures clearly decay with faster cooling rates.

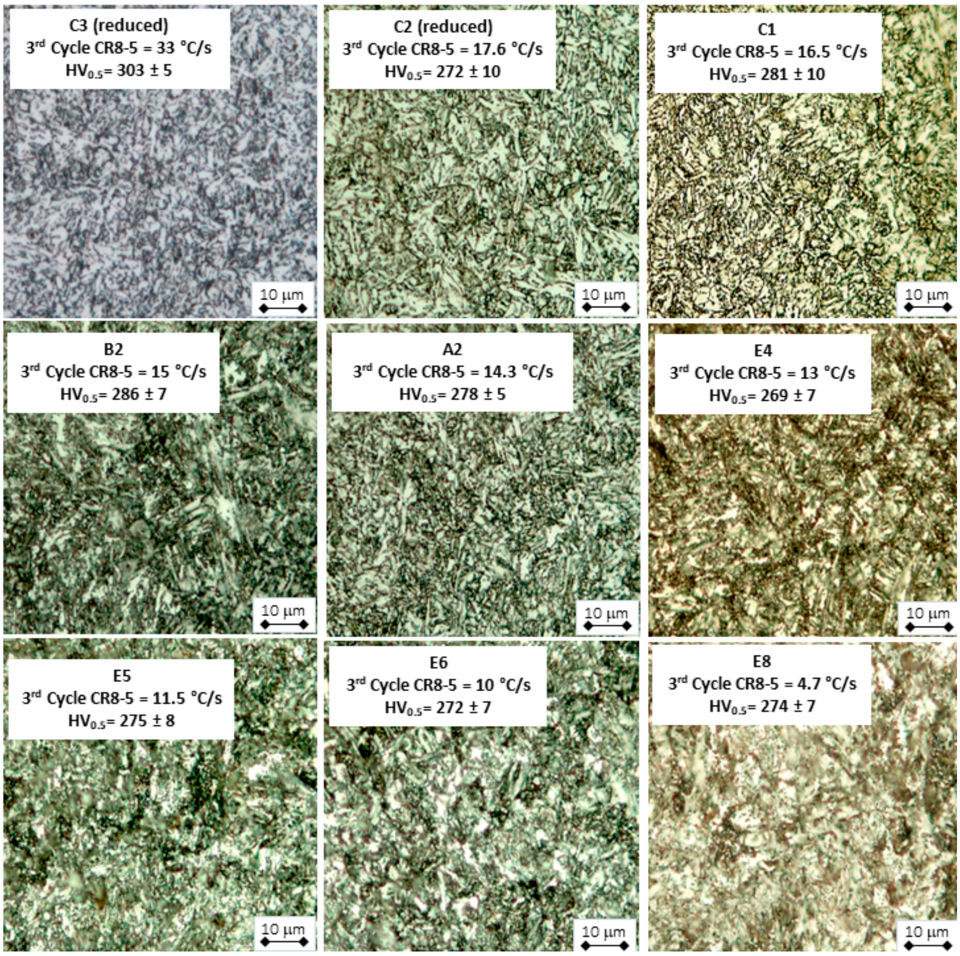

**Figure 6.** Central length cross-section OM micrographs of the specimens under different thermal cycles: decreasing cooling rates (CR8-5) and Vickers average microhardness (the 3rd cycle, with the programmed peak temperature of 800 °C, is the last one in which there is still phase transformation during heating).

**Table 4.** Gleeble physical simulations devised to measure the effect of multiple thermal cycles at different cooling rates between 800 and 500 °C (CR8-5) due to the third cycle.

| | | Austenitising (Heating) | | Transformation (Cooling) | |
|---|---|---|---|---|---|
| **Specimen** | **CR8-5 of 3rd Cycle (°C/s)** | **Start Temp (°C)** | **End Temp (°C)** | **Start Temp (°C)** | **End Temp (°C)** |
| C-3 (reduced) | 35.0 | 711 | 803 | 564 | 320 |
| C-2 (reduced) | 17.7 | 714 | 805 | 583 | 283 |
| C-1 | 16.5 | 724 | 810 | 557 | 297 |
| B-2 | 15.0 | 715 | 801 | 561 | 315 |
| A-2 | 14.3 | 699 | 800 | 557 | 298 |
| E-4 | 13.0 | 708 | 803 | 569 | 291 |
| E-5 | 11.5 | 713 | 807 | 547 | 281 |
| E-6 | 10.0 | 710 | 805 | 569 | 279 |
| E-8 | 4.6 | | | 565 | 278 |

### *4.2. The Effect of the Grain Size and Peak Temperature on the Position of the Transformation Curves*

Using numerical simulation through JMatPro®, Figure 7 shows that after a thermal cycle in which the peak temperature is close to the transformation temperature, the quenchability of the steel becomes less intensive. It means that the regions reheated close to the transformation temperature have a lower chance of being hardened by the formation of martensite. This is an outstanding point. As seen in Table 3, the programmed cooling rates reduce slightly from the 1st to the 3rd cycle. Together with a lower quenchability, the resulting microstructures after the 2nd and 3rd cycles tend to be softer than if the material undergoes only the 1st thermal cycle based on cooling rates (it must be stated that other factors can affect hardness). A similar trend was observed by Mičian et al. [22] in physical simulation with Gleeble. They showed that low-alloyed steel samples undergoing a thermal cycle with a temperature peak of 1350 °C showed larger grain sizes than those heated at 1200 °C.

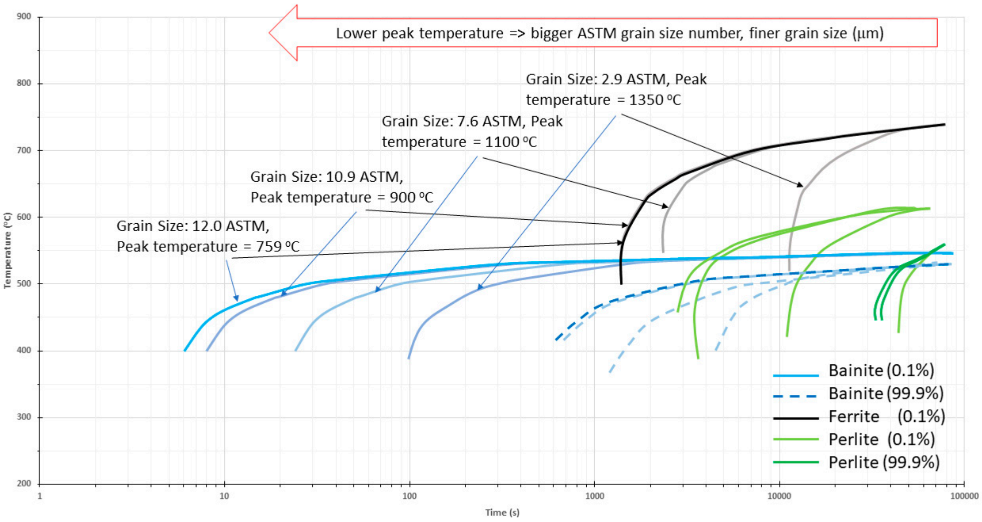

**Figure 7.** Superimposed outlined CCT diagrams from numerical simulation (JMatPro®), showing how the reducing peak temperatures (with paired hypothetic finer grains) affect the quenchability of the steel.

To confirm the numerical simulation results, Table 5 shows the metrics of the experiments regarding the progress of multiple thermal cycles. Recall that the specimens were submitted to the same thermal cycles employed in the Gleeble simulation of specimen A-2 (Table 3), but the first specimen with heating and cooling stopped after the 1st cycle, the second specimen (A-2 (2 cycles)) after the 2nd cycle, and the third specimen (A-3 (3 cycles)) after the 3rd cycle. The characteristics of the 3-cycle-sequential specimens were compared to those of specimen A-2 with the 4 cycles, concerning austenitising start and end temperatures during both heating and cooling periods, hardness, and microstructures. As seen, measured heating rates from 500 °C to the peak temperature decrease with the number of cycles (due to the Gleebe settings), standing around 500 °C/s during the 1st cycle (mimicking a 1st WAAM deposited layer) to 65–100 °C during the 3rd cycle (mimicking the sequential cycle after the 3rd layer). One must remember that peak temperatures also decreased from the 1st to the 3rd cycles, justifying the heating rate in the latter case. In turn, the cooling rates from 800 °C to 500 °C did not vary consistently with the number of cycles, staying around 13–17 °C/s at the 3rd cycle (the 4th cycle of specimen A-2 with the 4 cycles did not reach the transformation temperature).

**Table 5.** Gleeble physical simulations devised to measure the effect of progressive multiple thermal cycles (setting and heating and cooling-related metrics).

| | | | | Heating & Cooling Rates | | Austenitising (Heating) | | Transformation (Cooling) | |
|---|---|---|---|---|---|---|---|---|---|
| **Specimen** | **Remarks** | **Cycle Order** | **Peak Temp (°C)** | **500-Peak (°C/s)** | **800–500 (°C/s)** | **Start Temp (°C)** | **End Temp (°C)** | **Start Temp (°C)** | **End Temp (°C)** |
| A-2 (1 cycle) | A3 (only 1st cycle) | 1 | 1352 | 465.6 | 16.0 | 721 | 838 | 505 | 339 |
| A-2 (2 cycles) | A4 (1st + 2nd cycle) | 1 | 1351 | 472.8 | 17.5 | 727 | 843 | 508 | 339 |
| | | 2 | 1002 | 251.0 | 17.0 | 708 | 869 | 512 | 313 |
| A-2 (3 cycles) | A5 (1st + 2nd + 3rd cycle) | 1 | 1345 | 515.2 | 15.3 | 739 | 820 | 508 | 339 |
| | | 2 | 1003 | 251.5 | 18.8 | 729 | 861 | 507 | 284 |
| | | 3 | 801 | 100.3 | 15.8 | 716 | 802 | 560 | 312 |
| A-2 | A2 (1st + 2nd + 3rd + 4th cycle) | 1 | 1342 | 498.2 | 17.4 | 712 | 860 | 506 | 307 |
| | | 2 | 1011 | 176.8 | 15.0 | 695 | 867 | 502 | 292 |
| | | 3 | 802 | 65.2 | 13.0 | 699 | 800 | 550 | 290 |
| | | 4 | 609 | 27.3 | - | | | | |

Still from Table 5, the heating austenitising start temperatures oscillated from 699 to 739 °C, while the austenitising end temperatures (fully austenitic) varied from 802 to 869 °C. The transformation start temperatures during cooling are between 502 and 560 °C, while the transformation end temperatures range from 284 to 339 °C. In all cases, the temperature differences are due to the accuracy of the measurement of these quantities and also to the variation of the peak temperatures and heating rates among the tested specimens.

Figure 8 illustrates the optical micrographs at the centre of the specimens specified in Table 5, with the respective average Vickers microhardness. One can notice from (a) to (c) that the typical bainitic microstructure after the 1st cycle did not change too much after the 3rd cycle. A potential prior austenitic refinement can justify the trend for a slightly increasing hardness (the smaller, the harder). The microconstituent of the frame (d) and the hardness drop suggest the Bainite transformation was tempered by the 4th cycle (below any transformation during reheating). Therefore, the numerical simulation meets evidence in the experimental work that it represents the phenomenon of multiple cycles over the material.

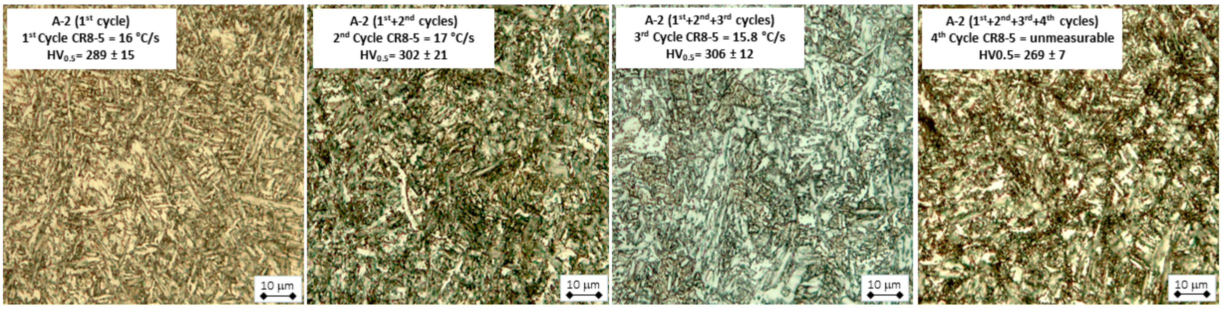

**Figure 8.** Central length cross-section OM micrographs of the specimens under subsequent progressive thermal cycles: cooling rates and Vickers average microhardness (the 3rd cycle, with a programmed peak temperature of 800 °C, is the last one in which there is still phase transformation during heating).

### 4.3. Forcing Cooling at Faster and Slower Rates than Feasible in the Experimental Gleeble Settings

Forced cooling (water shower, gas blow, etc.) was avoided on this experimental platform with Gleeble to prevent temperature gradients in the cross-sections where dilatometry would take place. Therefore, an intended variation of cooling rates was dependent only on the Gleeble jaw distance set and the specimen geometry. However, a minimal centre diameter (i.e., smaller than 4 mm) would lessen the dilatometry test sensitivity (4 mm was used in the reduced C-2 and C-3 specimens of Table 3). On the other hand, the results presented in Figure 6 and the simulated CCT diagram of Figure 7 indicate that much faster cooling would be necessary to have the material within the martensitic field—similarly, slower cooling would be necessary to demonstrate that this material could be transformed into ferritic and perlitic phases during very slow cooling from austenitic temperatures.

The solution to this downside was to submit the material from the wall to a furnace heat treatment. The intention of this solution was not to use the outcomes in the construction of the CCT diagram (different thermal cycles, no dilatometric measurement), but to demonstrate that by lowering the material temperature outside the range of cooling already applied in the Gleeble experiments (Section 4.1), it would match what was predicted in the numerical simulation (Figure 7). That is, martensite will predominate well above the maximum cooling rate of 18 °C/s and ferrite and perlite well below the minimal cooling rate of 4.5 °C/s. Thus, small samples were heated at 1100 °C for ≈100 min inside a furnace, and one sample was quenched in water (faster cooling rate), another normalised in atmospheric air (intermediate cooling rate), and the last one annealed inside the furnace (slowest cooling rate).

Figure 9 presents the resulting microstructures and corresponding average hardness of the material samples after the heat treatments. As seen, the aim of producing martensite was reached when the sample was quenched in water. Likewise, the sample aimed at getting ferrite and some perlite succeeded after annealing in a furnace. The normalised sample, with the intermediate cooling speed, is suggested by the bainitic microstructure and hardness level to be similar to most of the microstructures of Figure 6; the microstructure is somewhat coarse, justifying the slightly smaller hardness.

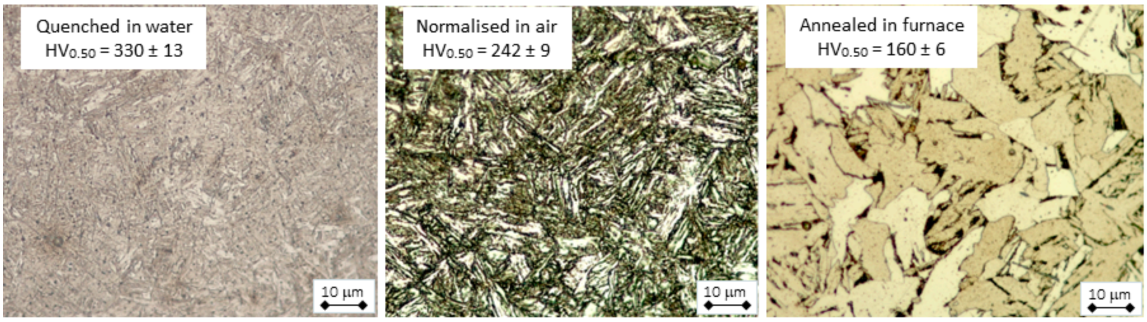

**Figure 9.** OM micrographs of the samples treated in a furnace (heated at 1000 °C × 10 min and quenched, normalised or annealed) with the Vickers average microhardness (20 indentations).

Using the same furnace heat treatment approach, the effect of the multiple cycles (progressively lower peak temperatures) on the microcomponents was also verified. Using the same furnace approach, four samples were heated at different peak temperatures and cooled in air at room temperature (normalisation). This cooling has proven in the previous stage to provide microstructures and hardness similar to those simulated by Gleeble. Figure 10 presents the resulting microstructures and corresponding average hardness of the material samples after the heat treatments. As seen, lower peak temperatures led to refined grains without changing the main constituents (still Bainite), but with progressively lower hardness. Only the microstructure of the sample that was heated only at 600 °C (below transformation temperatures) did not follow this trend. The original bainite from the wall material appears fragmented, with some carbide precipitations (a tempering effect). The hardness, consequently, is even lower.

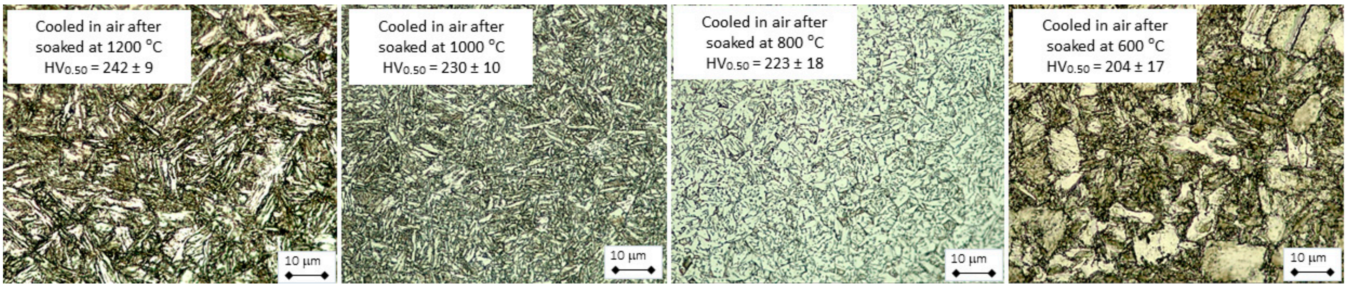

**Figure 10.** OM micrographs of the samples treated in a furnace (heated at different temperatures and cooled in air) with the Vickers average microhardness (20 indentations).

### *4.4. Building the CCT Diagram of the Steel under Study*

In Figure 11, all start and end transformation values from Table 4 were plotted according to the corresponding cooling rates after the material had undergone multiple thermal cycles. Even though a reasonably wide range (from approximately 4 to 33 °C/s) of cooling rates had been covered, and even though the furnace simulation approach has disclosed that faster and slower cooling speeds could change the microstructure to predominant martensitic or ferritic structures, respectively, the eight specimens used in the physical simulation with Gleeble were not enough to outline the transformation curves of a CCT diagram.

Therefore, JMatPro® numerical simulation was employed to assist in delineating the shape and position of the transformation curves, which are the essence of the CCT diagrams. It is well known that, besides the chemical composition, the austenitic grain size before cooling is a vital input (see Figure 7). Lan et al. [16] proposed that, besides the Hall–Petch strengthening effect, the carbon segregation at the fine austenite grain boundaries decreases the Bainite start temperature as a result of the increase in interfacial energy of nucleation. However, measuring or estimating prior austenitic grain sizes in materials under arc welding-like reheating is challenging. The proposal was to simulate the material numerically at the peak temperature of 800 °C using different estimated grain sizes as input parameters. As seen in Figure 12, when changing the input from an ASTM 15 grain size to an ASTM 3 grain size, the Bainite line changes from starting at approximately 7 s to 500 s (a remarkable difference).

By superimposing Figure 11 on each of the frames from Figure 12, one could say that a grain size of ASTM 15 better fits the transformations identified by dilatometry, yet not ideally (the start transformation times for Bainite from the numerical simulation matched the experimental results, but the start transformation temperatures were about 80–100 °C lower). It is important to say that the starting fraction used in Figure 12 calculations is 1%. If using 0.1% instead, bainite/pearlite/ferrite curves would be pushed higher. Consequently, the difference between the numerically closed, matched simulated bainitic transformation curve and the experimental data (Figure 11) would be narrower. Nevertheless, these transformation curves can be added to the semi-log plot, as seen in Figure 13. From this new figure, one can say, considering inaccuracies and uncertainties from both the experimental approach (mainly on the determination of the start and end transformation temperatures) and the numerical approach (mainly due to the temperature of austenitisation, inside the intercritical, or partially transformed, region for the steel under study), that the likely position of the Bainite and Martensite curves is within the range identified by a light grey colour. But there are other sources of uncertainties in the experimental determinations. For instance, the start and end of transformations measured by dilatometry would be impacted by specimen cross-section decarburisation. Aprilia et al. [23] recently published a study in which they concluded that decarburisation of the wall surface in Plasma Arc WAAM exists. However, in the case of this work, the potentially decarburised specimen surface is not expected since the specimens were machined to reach the nominal diameter of 6 mm.

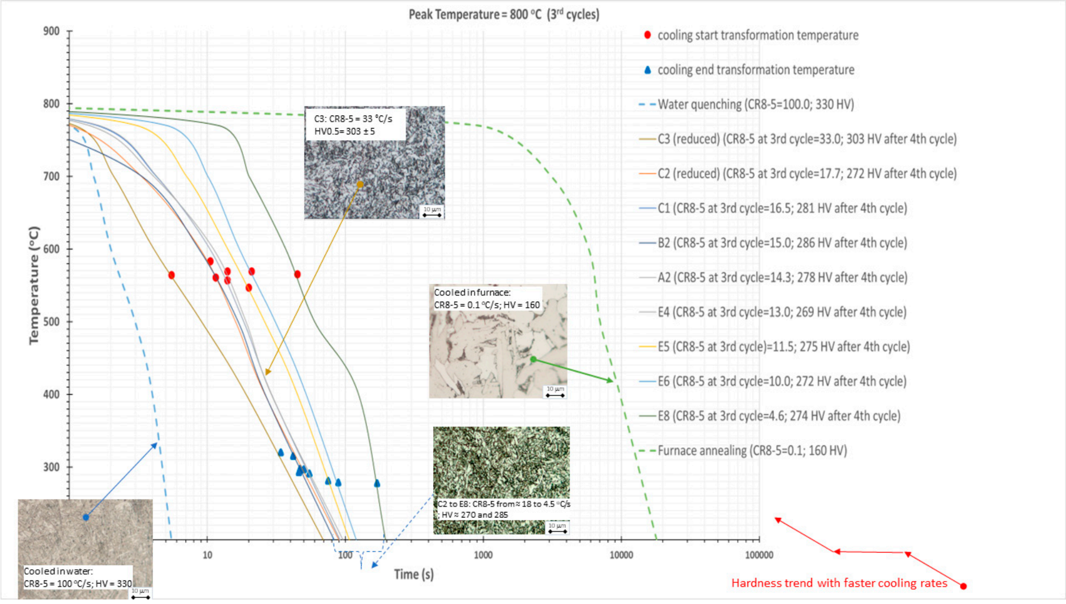

**Figure 11.** Semi-log plot of the start and end transformation temperatures as a function of time from different cooling rates.

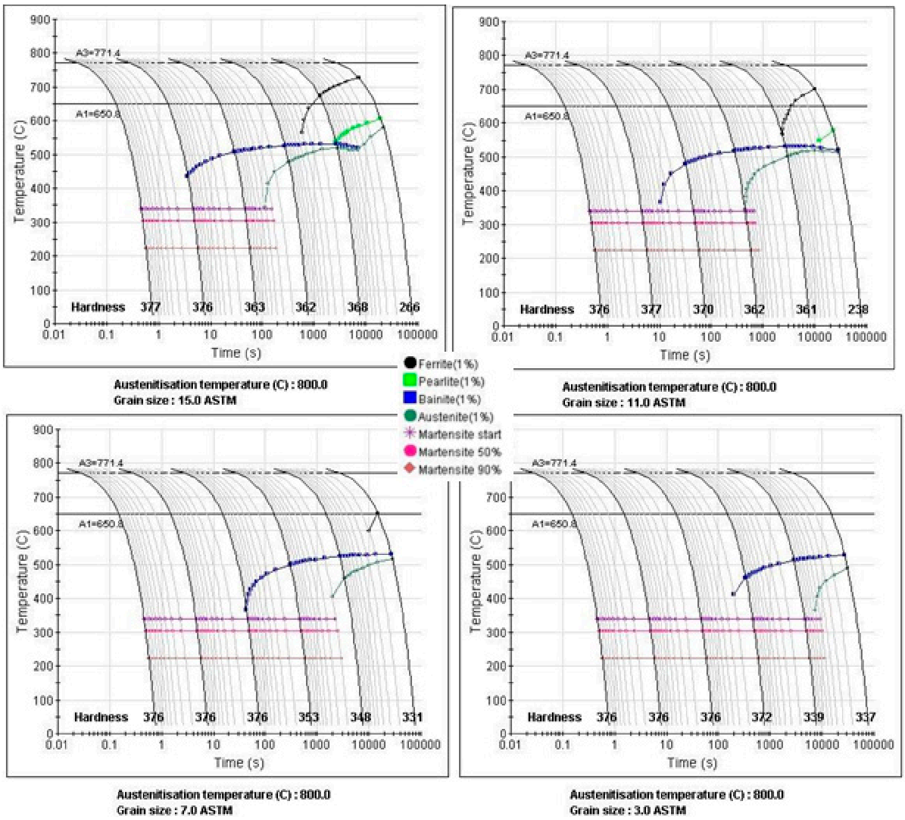

**Figure 12.** Plots of CCT simulation of the steel under study with a peak temperature of 800 °C and increasing grain sizes.

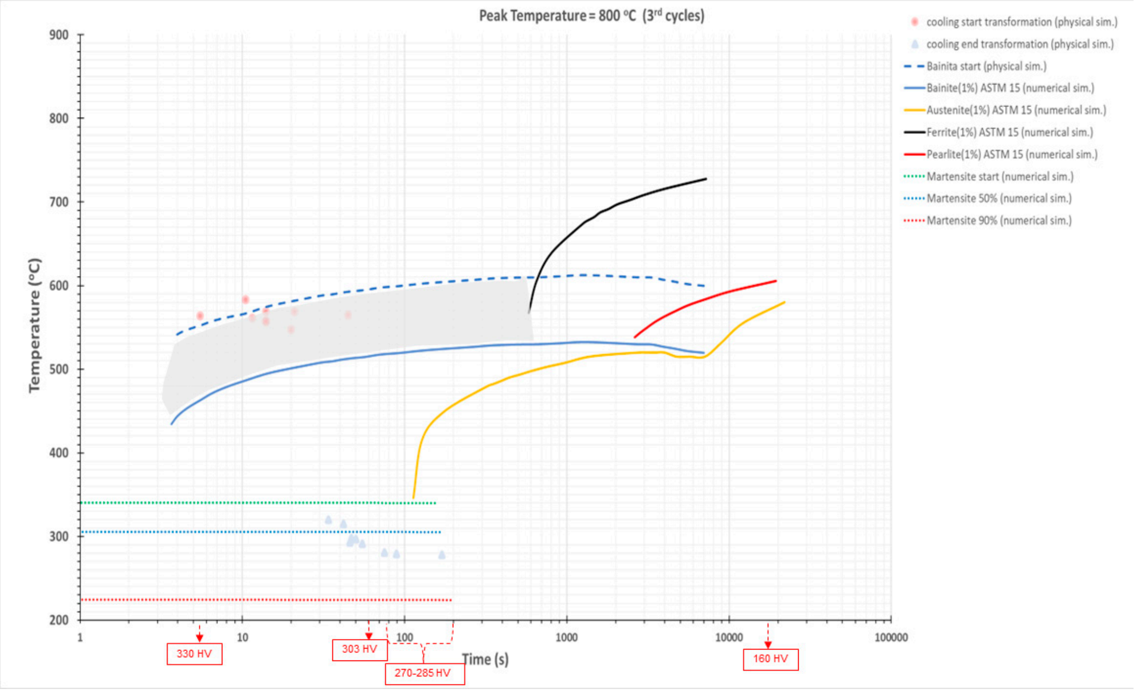

**Figure 13.** The combined numerically simulated CCT diagram (Figure 12), considering grain size ASTM 15, and physically simulated data (Figure 11), which compose the MC-CCT diagram of the thin wall material (metal-cored wire OK Tubrod 14.03, shielded by Ar + 5%$CO_2$) built by WAAM (layer after 4 sequential cycles with peak temperatures of 1300 °C, 1000 °C, 800 °C and 600 °C).

Anyhow, the most important information in a CCT diagram (and consequently, a MC-CCT diagram) is not the austenitic transformation curve positions in relation to the temperature axis but the final microstructures resulting from different cooling rates. Under this assumption, the shape and position of the transformation curve in relation to the time axis are important. In this regard, it is believed that Figure 13 fulfils the requirements of having precise information (transformation curve shape, hardness, and microstructure as a function of cooling rates).

It is noteworthy that, despite the representability of the resulting transformation curve ranges in Figure 13, the MC-CCT of this feedstock is due to the cooling rates of the 3rd cycle (peak temperature inside the intercritical region of the phase diagram of the given steel—Figure 1), but the final microstructures will be affected by the 4th cycle (peak temperature inside its subcritical region—Figure 1). As seen in Figure 3, during the 4th cycle (reinforced by subsequent cycles), there is no metallurgical transformation anymore. But hardness reduction and slight microstructure changes (due to a tempering effect) are justified, as shown in Figure 8. Similar results were observed by Mishra et al. [6].

It is also worth pointing out that the current MC-CCT was designed for deposition conditions in which the WAAM layers are heated at similar thermal cycles as here, typical of thin walls built up with the same layer parameters. The application of the same diagram in thicker walls or even deposited by another additive manufacturing technique (such as metal laser deposition) must be made with caution since the thermal cycles may create bands of maximum (peak) temperatures in the same layer. As seen in Figure 7 and Table 5, the start and end transformations may be modified according to the peak temperature.

## 5. Conclusions

In general, Table 5 shows that the start and end transformation temperatures are not impacted very much by the number of cycles (for this feedstock and cooling range). However, Figure 7 suggests a strong influence of the austenitic grain size on the position of the transformation curves in a time × temperature plot. In turn, grain sizes of a steel with a given composition are governed mainly by the peak temperature and the time length of stay above the transformation temperature (which in WAAM thermal cycles are affected by the heating time above this temperature, the peak temperature itself, and the cooling time before the transformation temperature). From another perspective, Figure 1 supports the idea that thin walls wire-arc additively manufactured will have most of the layers subjected to reheat treatment by subsequent thermal cycles at temperatures just above the austenitising temperature.

Therefore, it is reasonable to conclude that a WAAM MC-CCT diagram for a thin wall must be simulated by multiple cycles with decreasing peak temperatures. However, the thermal cycle cooling rate at which the peak temperature is the nearest to the austenitising temperature will govern the transformations during cooling (in the current case, the 3rd thermal cycle), although the following thermal cycles in which the peak temperature is within the range of tempering temperatures may affect the final microstructure and hardness (as seen in Figure 8).

Focusing on the objective of this work, it was also concluded that the methodology that combines physical simulations (for instance, using Gleeble® dilatometry) and numerical simulation (as using JMatPro®) allows building a comprehensive CCT diagram for the deposited material in thin wall WAAM of a given HSLA steel with a reasonably small number of experiments.

**Author Contributions:** Conceptualisation: A.S.; Methodology: M.H., J.A. and A.S.; Material preparation and data collection: M.H., A.F., A.R., P.L. and M.I.; Writing—original draft preparation: A.S.; Writing—review and editing: J.A.; Funding acquisition: J.A. All authors have read and agreed to the published version of the manuscript.

**Funding:** The Knowledge Foundation funded this research via the TAPERTECH: TAiloring of high-PERformance parts through laser and arc additive manufacturing TECHhnologies project (Reference number: 2018/1890 B20).

**Acknowledgments:** The authors are grateful to Eva-Lena Bergquist, representing ESAB AB, for supplying the consumables and machining the Gleeble specimens. Also to Sente Software Ltd., in particular to Zhanli Guo, for the support with the use of the JMatPro® software, ver. 13.0, Sente Software Ltd, Guildford, UK.

**Conflicts of Interest:** The authors declare no conflict of interest.

## References

1. Trzaska, J.; Jagiełło, A.; Dobrzanski, L.A. The calculation of CCT diagrams for engineering steels. *Arch. Mater. Sci. Eng.* **2009**, *39*, 13–20.
2. Alexandrov, B.T.; Lippold, J.C. In-Situ Weld Metal Continuous Cooling Transformation Diagrams. *Weld. World* **2006**, *50*, 65–74. [CrossRef]
3. Atkins, M. *Atlas of Continuous Cooling Transformation Diagrams for Engineering Steels*; Market Promotion Department, British Steel Corporation: London, UK, 1980.
4. Kellogg, F.; Vasilev, E.; Kudzal, A.; Taggart-Scarff, J.; Marsico, J.; Knezevic, M.; McWilliams, B. Physical simulations of heat-affected zone microstructures to compare weldability characteristics of additively manufactured and wrought 17-4 stainless steel. *Mater. Characterisation* **2022**, *185*, 111714. [CrossRef]
5. Halmešová, K.; Procházka, R.; Koukolíková, M.; Džugan, J.; Konopík, P.; Bucki, T. Extended Continuous Cooling Transformation (CCT) Diagrams Determination for Additive Manufacturing Deposited Steels. *Materials* **2022**, *15*, 3076. [CrossRef] [PubMed]
6. Mishra, V.; Babu, A.; Schreurs, R.; Wu, K.; Hermans, M.J.M.; Ayas, C. Microstructure estimation and validation of ER110S-G steel structures produced by wire and arc additive manufacturing. *J. Mater. Res. Technol.* **2023**, *23*, 3579–3601. [CrossRef]
7. Gutiérrez Castañeda, E.; Ruiz Cigarrillo, D.; Torres Castillo, A.; Salinas Rodríguez, A.; Deaquino Lara, R.; Bedolla Jacuinde, A.; Hernández Bocanegra, C. Intercritical continuous cooling transformation diagram for the manufacture of low-alloyed low-carbon multiphase steels. *Mater. Lett.* **2023**, *331*, 33528. [CrossRef]
8. Cruz-Crespo, A.; Araujo, D.B.; Scotti, A. Effect of Tempering Pass on HSLA-80 Steel HAZ Microstructures. *Weld. J.* **2013**, *92*, 304s–311s.
9. Zong, Y.; Liu, C.-M. Continuous Cooling Transformation Diagram, Microstructures, and Properties of the Simulated Coarse-Grain Heat-Affected Zone in a Low-Carbon Bainite E550 Steel. *Metals* **2019**, *9*, 939. [CrossRef]
10. Zachrisson, J. In Situ Detection and Characterisation of Phase Transformations in Weld Metals. Master's Thesis, Master of Science Programme, Engineering Physics, Luleå University of Technology, Luleå, Sweden, 2006; p. 44.

11. Moravec, J.; Mičian, M.; Málek, M.; Švec, M. Determination of CCT Diagram by Dilatometry Analysis of High-Strength Low-Alloy S960MC Steel. *Materials* **2022**, *15*, 4637. [CrossRef] [PubMed]
12. Guo, Z.; Saunders, N.; Miodownik, P.; Schillé, J.-P. Modelling phase transformations and material properties critical to the prediction of distortion during the heat treatment of steels. *Int. J. Microstruct. Mater. Prop.* **2009**, *4*, 187–195. [CrossRef]
13. Collins, J.; Piemonte, M.; Taylor, M.; Fellowes, J.; Pickering, E. A Rapid, Open-Source CCT Predictor for Low Alloy Steels, and Its Application to Compositionally Heterogeneous Material. *Metals* **2023**, *13*, 1168. [CrossRef]
14. Adonyi, Y.; Blodgett, O. Heat-affected zone characterisation by physical simulations. *Weld. J.* **2006**, *85*, 42–47.
15. Rakesh, R.; Ajit, K.N.; Kuldeep, K.S.; Velaphi, M. Physical simulation on Joining of 700 MC steel: A HAZ and CCT curve study. *Mater. Res. Express* **2022**, *9*, 046522. [CrossRef]
16. Lan, L.; Chang, Z.; Fan, P. Exploring the Difference in Bainite Transformation with Varying the Prior Austenite Grain Size in Low Carbon Steel. *Metals* **2018**, *8*, 988. [CrossRef]
17. Scotti, A.; Li, H.; Miranda, R.M. A Round-Robin Test with Thermal Simulation of the Welding HAZ to draw CCT diagrams: A need for harmonised procedures and microconstituent terminologies. *Soldag. Insp.* **2014**, *19*, 279–290. [CrossRef]
18. Barrick, E.J.; Jain, D.; DuPont, J.N.; Seidman, D.N. Effects of Heating and Cooling Rates on Phase Transformations in 10 Wt Pct Ni Steel and Their Application to Gas Tungsten Arc Welding. *Metall. Mater. Trans. A* **2017**, *48*, 5890–5910. [CrossRef]
19. Krbat'a, M.; Majerík, J.; Barényi, I.; Ecker, M. Experimental determination of continuous cooling transformation diagram for high strength steel OCHN3MFA. *Mater. Sci. Eng.* **2020**, *776*, 012095. [CrossRef]
20. Kardoulaki, E.; Lin, J.; Balint, D.; Farrugia, D. Investigation of the effects of thermal gradients present in Gleeble high-temperature tensile tests on the strain state for free cutting steel. *J. Strain Anal. Eng. Des.* **2014**, *49*, 521–532. [CrossRef]
21. Bhadeshia, H.K.D.H. *Bainite in Steels: Theory and Practice*, 3rd ed.; Maney Publishing: Leeds, UK, 2015; p. 589. ISBN 978-1-909662-74-2.
22. Mičian, M.; Winczek, J.; Harmaniak, D.; Koňár, R.; Gucwa, M.; Moravec, J. Physical Simulation of Individual Heat-Affected Zones in S960mc Steel. *Arch. Metall. Mater.* **2021**, *66*, 81–89. [CrossRef]
23. Aprilia, A.; Zhai, W.; Guo, Y.; Aishwarya; Shandro, R.; Zhou, W. Decarburization of Wire-Arc Additively Manufactured ER70S-6 Steel. *Materials* **2023**, *16*, 3635. [CrossRef] [PubMed]